JET-P(95)27

Modelling of Lower Hybrid Current Drive and Comparison with Experimental Results in JET

Y F Baranov, A Ekedahl, P Froissard[1], C Gormezano,
M Lennholm, F Rimini, F X Söldner.

JET Joint Undertaking, Abingdon, Oxfordshire, OX14 3EA, UK.
[1] Association Euratom-CEA/DRFC, CEN Cadarache, 13108 Saint-Paul-lez durance, Cedex.

Preprint of a paper to be submitted for publication in
Nuclear Fusion

July 1995

ABSTRACT.

A new code has been developed and benchmarked with data from Lower Hybrid current drive (LHCD) experiments in JET. The model includes stochastic radial diffusion of electrons and scattering of lower hybrid waves. The code is validated by comparing calculated and experimental current drive efficiencies as well as calculated and measured hard X-ray bremsstrahlung emission radial profiles. Reasonable agreement has been found for full LH current driven cases and LH plus moderate DC electric field.

INTRODUCTION

Lower hybrid current drive is one of the most promising methods of profile control and current sustainment in a tokamak reactor. It has the highest current drive efficiency and its potentiality is proven and established with a wide data base from a large number of experiments. Modelling of LHCD scenarios in a reactor requires the development of a reliable code based on an adequate physical model. Propagation and absorption of LH waves, interaction of the fast electrons with the RF field and their spatial diffusion are the most important phenomena, which should be treated properly. The ray-trajectory approach was used to simulate propagation and absorption of lower hybrid waves by a number of authors [1-11]. The WKB method was generalised for the description of lower hybrid waves in the electrostatic approximation in [12] and the diffraction effects were taken into account. The effect of the LH wave scattering by quasistatic fluctuations in tokamaks was investigated in [1,13]. The evolution of the electron distribution function in the presence of LH waves can be described by a 2D (in the momentum space) Fokker-Planck equation (FPE) in a homogeneous plasma [14]. An approximate solution can be obtained from a 1D (in the momentum space) FPE by introducing a perpendicular temperature of the electron tail [15]. In plasmas with a density in the range $1\text{-}3*10^{19}$ m^{-3} the spatial diffusion may be important [16,17]. An interaction of electrons with LH waves and their spatial diffusion can be described by 2D [16] or 3D [18] FPE.

The LHCD code, described in the present work, is based on the ray-tracing approach for the description of LH waves propagation. Scattering of LH waves by low frequency density fluctuations is taken into account and treated by the Monte-Carlo method. Quasilinear and spatial diffusion of the fast electrons are described by a 2D (parallel momentum and radial coordinates) FPE. The effect of pitch angle scattering is included by introducing an effective perpendicular temperature of the tail. The solution of the FPE is then used to calculate the X-ray emission by the suprathermal electrons.

The verification of the model relevant to LHCD requires local measurements of the power spectrum of LH waves. Current profile measurements are only occasionally available

in a few experiments [19,20,**21**]. The Fast Electron Bremsstrahlung (FEB) diagnostic on JET [22,**23**] provides unique information about energy and spatial distribution of fast electrons carrying the LH driven current. Comparison of the calculated X-ray emission spectra and profiles with experimental data is used in this work for the validation of the model and the code.

This paper is organised as follows. The ray-tracing approach employed in the code is described in section 1. Section 2 is devoted to a brief description of the LH wave scattering model. The 2-D Fokker-Planck equation is introduced in section 3. Interaction of different parts of the code is explained in section 4. General features of the FEB diagnostic and the method of hard X-ray emission calculation is given in section 5. Section 6 is devoted to the code validation. Results of modelling with analysis of experimental data are presented in section 7. Prediction of LHCD in ITER is described in section 8.

I. LH WAVE PROPAGATION

The ray-trajectory method is employed to simulate propagation and absorption of lower hybrid waves. The equations describing the ray trajectory of a wave can be written as follows[6]:

$$\frac{d\rho}{dt} = -\frac{\partial D/\partial k_\rho}{\partial D/\partial \omega} \qquad \frac{d\theta}{dt} = -\frac{\partial D/\partial k_\theta}{\partial D/\partial \omega} \qquad \frac{d\zeta}{dt} = -\frac{\partial D/\partial k_\zeta}{\partial D/\partial \omega}$$

$$\frac{dk_\rho}{dt} = \frac{\partial D/\partial \rho}{\partial D/\partial \omega} \qquad \frac{dk_\theta}{dt} = \frac{\partial D/\partial \theta}{\partial D/\partial \omega} \qquad \frac{dk_\zeta}{dt} = \frac{\partial D/\partial \zeta}{\partial D/\partial \omega} \tag{1}$$

Here (ρ,q,ζ) are a special set of coordinates, in which magnetic surfaces are described by the condition r=const. The equilibrium is described by the three-moment approximation, which takes into account the Shafranov shift, the ellipticity and triangularity of the magnetic surfaces. Than we can introduce the following relation between (ρ,q,ζ) and the cylindrical coordinate system (r,ϕ,z):

$$\begin{aligned} r &= R_0 - \Delta(\rho) + \rho\cos(\theta) - \gamma(\rho)\sin^2(\theta) \\ \phi &= \zeta \\ z &= \lambda(\rho)\rho\sin(\theta) \end{aligned} \tag{2}$$

where R_o is the radius of the magnetic axis, $\Delta(\rho)$-the Shafranov shift, $\lambda(\rho)$ the ellipticity and $\gamma(\rho)$ the triangularity of the magnetic surface. In the set of equations (1) k_ρ, k_θ,and k_ζ are canonically conjugate momenta, which are connected with longitudinal $n_{//}$ and transverse $n_\perp$ components of the refractive index through the relations:

$$n_{//}^2 = \frac{c^2}{\omega^2}\left[\frac{k_\theta^2 \sin^2\alpha}{g_{22}} + \frac{2k_\theta k_\rho \sin\alpha\cos\alpha}{\sqrt{g_{22}g_{33}}} + \frac{k_\rho \cos^2\alpha}{g_{33}}\right]$$
$$n_\perp{}^2 = \frac{c^2}{\omega^2}\left[\frac{k_\rho^2 g_{22} - 2k_\rho k_\theta g_{12} + k_\theta^2 g_{11}}{g_{11}g_{12} - g_{12}{}^2} + \frac{k_\zeta{}^2}{g_{33}{}^2}\right] - n_{//}{}^2 \qquad (3)$$

where g_{ik} are the components of the metric tensor, α is the angle between the toroidal direction and the direction of the total magnetic field, ω is the wave frequency and c is the speed of light. The dispersion relation for LH waves includes the electromagnetic part and thermal corrections.

$$D(\omega, n) \equiv \delta n_\perp{}^6 + A n_\perp{}^4 + B n_\perp{}^2 + C = 0$$
$$A = \varepsilon, \quad B = (\eta + \varepsilon)(\varepsilon - n_{//}{}^2)^2 - g^2, \quad C = \eta((\varepsilon - n_{//}{}^2)^2 - g^2),$$
$$\varepsilon = 1 + (\omega_{pi}/\omega)^2 - (\omega_{pe}/\omega_{ce})^2(1 - i\nu_{ei}/\omega), \quad g = -\omega^2{}_{pe}/\omega\omega_{ce}, \qquad (4)$$
$$\eta = 1 - (\omega_{pi}/\omega)^2 - (\omega_{pe}/\omega)^2(1 + i\pi(mc\omega/n_{//})^2\,\partial F(p_{//})/\partial p_{//} + \nu_{ei}/\omega),$$
$$\delta = -3((\omega_{pi}/\omega)^2(T_i/Mc^2) + 0.25(\omega\omega_{pe}/\omega^2{}_{ce})^2(T_e/mc^2))$$

where $T_{e,i}$ are electron or ion temperature, $p_{//}$ parallel momentum and $F(p_{//})$ is the electron distribution function defined in the next section. The absorption of power flowing along the ray path due to collisional and Landau damping by electrons is described by the equation

$$\frac{dP}{dt} = 2\gamma_e P \qquad (5)$$

where γ_e is determined by

$$\gamma_e = \frac{\mathrm{Im}\, D(\omega, k)}{\partial\, \mathrm{Re}\, D(\omega, k)/\partial\omega} \qquad (6)$$

The ray equations (1) and (5) were integrated numerically with the accuracy $(n_\perp - n_{\perp o})/n_\perp < 10^{-5}$, where $n_\perp$ and $n_{\perp o}$ are the results of integration and local solution of the dispersion relation, respectively.

The quasi linear diffusion coefficient can be calculated according to the following procedure. Let us assume that lower hybrid waves are launched by the antenna at the edge of the plasma with power spectrum $P(k^o_{//})$. During the propagation along the ray trajectory the energy density of the wave having local value $k'_{//}$ when it crosses magnetic surface $\rho=\rho'$ with an area S can be expressed in the terms of the RF energy density $W(k^o_{//}, k'_{//}, \rho')$ and the radial component of the group velocity $v_{g\rho}$

$$W(k^o_{//}, k'_{//}, \rho') = P(k^o_{//}, k'_{//}, \rho')/(S\, v_{g\rho}) \qquad (7)$$

Restricting ourselves to the cold plasma approximation and assuming that the RF power propagates in the form of the slow wave we can express the contribution to the quasi linear diffusion coefficient averaged over the magnetic surface as follows [1]:

$$\Delta D_{ql}(v,\rho')\big|_{v=\omega/k_{//}} = \frac{8\pi^2 e^2 k_{//}'^2 P(k_{//}^o, k_{//}', \rho')}{(k_{//}'^2 + k_{\perp}^2)(1+(\omega_{pe}/\omega)^2) S v_{g\rho}} \tag{8}$$

2. SCATTERING OF THE LOWER HYBRID WAVES

Scattering of the slow LH waves by low frequency density fluctuations is taken into account using a theory proposed by Ott [24]. No systematic measurements have been done on the fluctuation spectrum in JET. Gaussian like spectra were observed in Alcator C [25] and in several other tokamaks [26]. In our simulations the spectrum of fluctuations is approximated by a Gaussian function

$$S(k) = (1/\pi k_0^2)\langle \delta n/n \rangle^2 \exp(-(k/k_0)^2), \tag{9}$$

where k is the wave vector of the fluctuations, which is perpendicular to the magnetic field. The characteristic wave scale length k_0^{-1} is assumed to be of the order of the ion Larmor radius ρ_i (all calculations were carried out for $k_0^{-1} = 3\rho_i$). The mixing length theory [26] predicts a density fluctuation level given by: $\delta n/n \sim \sqrt{T_e/T_i}\, k_0^{-1}/L_n$, where $L_n = |d \ln n/dx|$. The spatial distribution of the fluctuation amplitude was adopted, for simplicity, in the form:

$$\langle \delta n/n \rangle^2 = \Delta(\rho\rho_i/a^2)^2, \tag{10}$$

where ρ is the radial coordinate and a the minor radius. The parameter Δ is introduced to investigate the influence of the fluctuation amplitude on the distribution of the driven current. The best agreement between the experimental data and results of calculations is observed (as discussed later) for

$$0.25 < \Delta < 1. \tag{11}$$

Like mode scattering (slow wave into slow wave) by density fluctuations rotates $k_{\perp}$ around the magnetic field B and does not change the magnitude of $k_{//}$. The scattering length l_s can be defined as the distance the wave must propagate in order to deflect its $k_{\perp}$ by an angle of 90°. The scattering length l_s for a slow wave with a group velocity perpendicular to the magnetic field $v_{g\perp}$ can be calculated according to [24] (see for more details also [1,13]):

$$l_s = {}^{v_{g\perp}}\!/_{\nu_l}$$

$$\nu_l = 2\int_0^{2\pi} K(k_\perp,\beta)S(k_\perp \sin(\beta/2))\sin^2(\beta/2)d\beta \qquad (12)$$

$$K(k_\perp,\beta) = \frac{\pi k_\perp \omega^2}{2v_{g\perp}} \frac{(((\varepsilon-1)\cos\beta+1)^2+g^2\sin^2\beta)^2}{1+(\omega_{pe}/\omega_{ce})^2}$$

Scattering of the waves is modelled in the framework of the ray-trajectory approach using the Monte Carlo method. We adopted a simplified version of the procedure, employed for the investigation of the effect of magnetic and density fluctuations on the propagation of LH waves in [13]. It is assumed that during each small step $ds \ll l_s$ along the trajectory $k_\perp$ is deflected by an angle $\Delta\Theta = \pi/2\sqrt{ds/l_s}$ with the average value $<\Delta\Theta>=0$. Each act of scattering conserves $k_\perp$ but it changes k_ζ, the ray trajectory, the behaviour of $\vec{k}$ along the trajectory and, as a result, the power spectrum in the plasma.

3. FOKKER-PLANCK EQUATION

The electron distribution function can be described by the relativistic 3D FPE[18]. It's solution requires a time consuming procedure. Our aim is to reconstruct the main feature of the solution of the 3D FPE distribution function using relativistic 2D FPE (in $p_{//}$ and ρ). Namely, our solution should approximately reproduce the current drive efficiency and the broadening of the 'tail' in the momentum space in the direction perpendicular to the magnetic field. In addition we want to take into account the spatial diffusion of the electron 'tail'. It should be noted that in the framework of the 2D ($p_{//}$ and ρ) approach we can not describe properly many details such as, for example, the deviation of the distribution function from a Maxwellian in perpendicular_direction, the increase of the fast electron tail with negative parallel momentum, the fine structure at the beginning of the plateau region [14].

The electron distribution function $F(p_{//},\rho)$ is calculated via a numerical solution of the relativistic 2D (in $p_{//}$ and ρ) Fokker-Planck equation :

$$\frac{\partial F(p_{//},\rho)}{\partial t} = \frac{\partial}{\partial p_{//}} D_{ql}(p_{//},\rho)\frac{\partial F(p_{//},\rho)}{\partial p_{//}} + \nu'_0 \frac{\partial}{\partial p}\frac{p_c^3}{p_{//}^3}\left[p_{//}F(p_{//},\rho) + \frac{T(p_{//},\rho)m\partial F(p_{//},\rho)}{\partial p_{//}}\right] + \frac{1}{\rho}\frac{\partial}{\partial \rho}\rho D_{\rho\rho}(p,\rho)\frac{\partial F(p_{//},\rho)}{\partial \rho} + eE(\rho)\frac{\partial F(p_{//},\rho)}{\partial p_{//}} \qquad (13)$$

where $p_{//}$ is the parallel momentum, ρ the radial coordinate , m the electron rest mass, $E(\rho)$ the toroidal electric field, ν'_0 the effective electron collisional frequency, $T(p_{//}, \rho)$ the parameter characterising the slope of the distribution function in the $p_{//}$ space, $D_{ql}(p_{//},\rho)$ and $D_{\rho\rho}(p_{//},\rho)$ are the quasilinear and spatial diffusion coefficients, respectively.

1D and 2D theory [27] predict, respectively, $(2+Z_{eff})^{-1}$ and $(5+Z_{eff})^{-1}$ dependence of the current drive efficiency on the effective ion charge Z_{eff}. To reconcile the 1D solution with a prediction of the 2D theory we introduce the effective collisional frequency

$$\nu_{ei}' = C_1(5+Z_{eff})\omega_{pe}^4 \log\Lambda/(8\pi n_e v_e^3), \tag{14}$$

where n_e is the electron density. The factor C_1=0.55 was chosen from the comparison of the simulated current drive efficiency and hard X-ray emission with the experimental quantities. It should be noted that from a comparison of two- and one-dimensional non relativistic calculations C_1=0.4 [14].

The fast 'tail' of the electron distribution function is spread in the perpendicular direction due to pitch angle scattering. It was shown in [15] that the electron distribution (in $p_\perp$) can be approximated by a Maxwellian with the perpendicular temperature

$$\tilde{T}_\perp(\rho) = T_e(\rho)\frac{g-1}{g+1}\left[\frac{v_1^{2-g}\left(v_2^{g+1}-v_1^{g+1}\right)-v_1^2(v_2-v_1)}{2(g-1)(v_2-v_1)-v_1^{2-g}(v_2^{g-1}-v_1^{g-1})}\right], \tag{15}$$
$$g = 2(1+Z_{eff})/(2+Z_{eff})$$

where v_1 and v_2 are the lower and upper boundary of the parallel phase velocity of the LH waves. Hard X-ray emission and it's radiation temperature are sensitive to $T_\perp$ [23]. Our simulations of hard X-ray emission showed that a distribution with $T_\perp$ from (16) produces usually a higher level of emission in the energy range $\hbar\nu \le 150$keV and a lower level of radiation temperature than in the experiment. We found that better agreement of experimental and simulated results can be achieved for $T_\perp$ gradually increasing from low values $T_\perp << \tilde{T}_\perp$ with $p_{//}$ in the plateau region. It is impossible to deduce the exact dependence of $T_\perp$ on $p_{//}$ from four energy channels of the line integrated FEB signal. For simplicity the perpendicular temperature has been chosen in the form:

$$T_\perp(p_{//},\rho) = \max(T_e, C_2\tilde{T}_\perp(\rho)((p_{//}/\gamma - v1)/(v2-v1))^2), \text{ for } v_1(\rho)<p_{//}/\gamma<v_2(\rho) \tag{16}$$

$$T_\perp(p_{//},\rho) = C_2\tilde{T}_\perp(\rho), \text{ for } p_{//}/\gamma>v_2(\rho),$$

where $\gamma = (1+p_{//}^2/(mc)^2)^{1/2}$.

The parameter $T(p_{//},\rho)$ in eq.(10) characterises the bulk electron temperature and it was chosen to be $T(p_{//},\rho) = T_e(\rho)$ for $p_{//}/\gamma < v_2(\rho)$. (In the plateau region the behaviour of $F(p_{//},\rho)$ is dominated by the quasilinear term under the condition $D_{ql}(p_{//},\rho)p_{//}^3 > \nu_{ei}' p_e^5$). From numerical simulations [14,28] it follows that the distribution function has similar slopes in $p_\perp$ and $p_{//}$ directions for high $p_{//}/\gamma > v_2$. In this region the parallel tail temperature was approximated by $T(p_{//},\rho) = C_2\tilde{T}_\perp(\rho)$.

It is assumed that the diffusion of the fast electrons is connected with the stochasticity of the magnetic field. In the framework of this model $D_{\rho\rho} = D_m\, p_{//}/(\gamma v_e)$. The typical value of D_m was chosen to be 0.5 m^2/s (as discussed later).

The distribution function must satisfy the following boundary conditions:

$$F(p_{//},\rho)\big|_{p_{//}=0} = \frac{n_e(\rho)}{\sqrt{2\pi}p_e(\rho)}, \qquad F(p_{//},\rho)\big|_{p_{//}\to\pm\infty} = 0,$$
$$\left.\frac{\partial F(p_{//},\rho)}{\partial\rho}\right|_{\rho=0} = 0, \qquad F(p_{//},\rho)\big|_{\rho=a} = \frac{n_e(a)\exp(-(p_{//}/p_e(a))^2)}{\sqrt{2\pi}p_e(a)} \tag{17}$$

The current generated by the lower hybrid waves is determined by

$$J_{RF}(\rho) = \int_{-\infty}^{+\infty} dp_{//}(F^1(p_{//},\rho) - F^0(p_{//},\rho)), \tag{18}$$

where $F^o(p_{//},\rho)$ and $F^1(p_{//},\rho)$ are the distribution functions calculated for zero and non-zero $D_{ql}(p_{//},\rho)$, respectively.

The RF power absorbed by fast electrons due to Landau absorption is equal to

$$P_{RF}(\rho) = \int_{-\infty}^{+\infty} (\gamma - 1)\frac{\partial}{\partial p_{//}} D_{ql}(p_{//},\rho)\frac{\partial F(p_{//},\rho)}{\partial p_{//}} dp_{//} = -\frac{1}{m}\int_{-\infty}^{+\infty} \frac{p_{//}}{\gamma} D_{ql}(p_{//},\rho)\frac{\partial F(p_{//},\rho)}{\partial p_{//}} dp_{//}. \tag{19}$$

The set of equations (13-17) does not describe the effect of runaway electrons properly. It is not applicable in the case when the parallel phase velocity of the waves in the plasma reaches the Dreicer velocity. In some cases this situation occurs in the peripheral part of the discharge. The local value of the electric field $E(\rho)$ is decreased for such cases. Calculations show that this decrease does not induce a large error, since the number of the fast electrons driven in this area is relatively small.

4. CODE STRUCTURE AND CALCULATION PROCEDURE

The LHCD code consists of three major interconnected parts: equilibrium, ray-tracing and Fokker-Planck codes. The magnetic field topology is simulated by a three moments equilibrium code, developed by Zakharov [29]. The poloidal magnetic field $B_p(\rho)$ and the functions $\Delta(\rho)$, $\gamma(\rho)$ and $\lambda(\rho)$ from equation (2) are calculated for given boundary values $\gamma(a)$, $\lambda(a)$, (a is the minor tokamak radius) central safety factor q_o and internal inductance l_i. Parameters $\gamma(a)$, $\lambda(a)$, q_o and l_i are taken from JET Processed Pulse File (PPF) data. They are obtained by the equilibrium reconstruction code existing at JET [30].

The wave spectrum $P(n_{//})$ for lower hybrid waves launched by the antenna is calculated independently by the SWAN code [31]. Standard $P(n_{//})$ is used for the simulations of all shots analysed in JET. For $\pi/2$ antenna phasing the full width between minima of the main lobe of the spectrum is $\Delta n_{//}=0.92$ and $n_{//}\approx 1.85$ corresponds to the maximum of $P(n_{//})$.

The spectrum $P(n_{//})$, magnetic field $B_p(\rho)$ and geometry characteristics $\Delta(\rho)$, $\gamma(\rho)$, $\lambda(\rho)$ are the input functions of the ray-tracing code. All relevant parameters ($T_e(\rho)$,$n_e(\rho)$, Z_{eff}) are taken from experimental data. Only the positive part of the spectrum in the range $1.45\leq n_{//}\leq 5$ is taken into account for LHCD simulations in JET. It is divided into 89 equal intervals. To simulate the poloidal height of the grill the ray trajectories are launched from K different poloidal positions ($25< K <40$). An initial power $P(n_{//})/K$ is prescribed to each launched ray. The quasi-linear diffusion coefficient is calculated according to equation (8). Data required for calculation of ΔD_{ql} are stored for each trajectory.

The Fokker-Planck equation (13) is solved numerically. The quasi-linear diffusion coefficients obtained by the ray-tracing code as well as profiles $T_e(\rho)$, $n_e(\rho)$, $E(\rho)$ and Z_{eff} are the input parameters to the Fokker-Planck code. A grid with 399 points in the velocity space and 41 radial points is chosen for the numerical solution of the Fokker-Planck equation.

The ray tracing and Fokker-Planck equation are calculated iteratively to get the stationary solution. The first iteration begins with the calculation of the decrement of the wave absorption in a target plasma with a Maxwellian velocity distribution. The electron distribution function, which is found in the n-th iteration is used for the calculation of $J^n_{RF}(\rho)$, $P^n_{RF}(\rho)$ and γ^n_e. The decrement γ^n_e determines the absorption of the waves and D_{ql} in the next iteration. The current profile $J_{RF}(\rho)$ is used for the check of the convergence of the solution. It converges if the spatial diffusion is taken into account ($D_m=0.5m^2/s$). Function $J_{RF}(\rho)$ is smooth in this case. Typically, the condition $\max\left|(J^n_{RF}(\rho)-J^m_{RF}(\rho))/J^n_{RF}(\rho)\right| < 0.1$ is satisfied for $m,n\geq 3$. For most cases the number of iterations is limited to three or four. Note that in the case with $D_m=0$ there is a convergence of the average current $J_{RF}(\rho)=n^{-1}\sum_n J^n_{RF}(\rho)$. Each particular realisation $J^n_{RF}(\rho)$ is not a smooth function of ρ and it changes from iteration to iteration. Simulations with a different number of launched rays show, that the greater the number of rays, the smoother the current $J^n_{RF}(\rho)$ and the smaller it's variation from iteration to iteration. Usually when simulations with $D_m=0$ are done, a condition $\max\left|(J_{RF}(\rho)-J^m_{RF}(\rho))/J^m_{RF}(\rho)\right| < 0.2$ is fulfilled for $m=4$. For practical reasons, the number of iterations is limited to 4 in this case. Note that the calculation of quasilinear diffusion coefficients can be simplified if all relevant parameters for each trajectory have been stored during the first iteration in the case without scattering. With scattering the next ray tracing iteration represents a new realisation of a random process. The

fact that there is a convergence indicates that each realisation is representative and validates Monte Carlo solution.

SIMULATION OF FAST ELECTRON BREMSSTRAHLUNG DATA

The Fast Electron Bremsstrahlung (FEB) diagnostic is a multichord system designed to detect hard X-ray emission from 100 keV upwards [22,23]. It consists of a horizontal and a vertical camera viewing a poloidal cross-section of the plasma with 10 and 9 lines of sight, respectively. The layout of the diagnostic is shown in Fig.1. The distance between adjacent lines of sight, as taken in the plasma centre, is around 19 cm for the vertical camera and 22 cm for the horizontal camera. The detector boxes are shielded from background γ and neutron fluxes by high density concrete and lead shielding. Signal detection is done with a 10x10x15 mm CsI(Tl) detector equipped with photo diodes. The signal integration time is typically set to 10 ms. For each line of sight, the X-ray emission spectrum is analysed on 4 equal energy windows between 100 and 300 keV to produce 4 line integrated emissivity profiles. By analogy with the thermal bremsstrahlung emission, the slope of the hard X-ray intensity spectrum is used to calculate a photon temperature, which provides an indication on the suprathermal electron population. The introduction of the photon temperature is justified by the hard X-ray emission spectra measurements. These measurements were carried out for a number of shots with the aim of pulse height analysis diagnostic (PHA) [39]. They show that the slope of the hard X-ray intensity spectrum can be characterised approximately by one temperature in the photon energy range $100keV \le h\nu \le 300keV$.

The FEB signal is calculated using the simulated electron distribution function. The local suprathermal emissivity for a photon of an energy ε at an angle ϑ with respect to the local magnetic field direction is given by:

$$\frac{d^4N(\varepsilon,\vartheta,\rho)}{d\varepsilon dV dt d\Omega} = \iiint d^3\mathbf{p} v_s f_s(\mathbf{p},\rho)\left[\sum_i Z_i^2 n_i(\rho)\frac{d^2\sigma_{ei}(\mathbf{p},\varepsilon,\vartheta,Z_i)}{d\varepsilon d\Omega} + n_e(\rho)\frac{d^2\sigma_{ee}(\mathbf{p},\varepsilon,\vartheta)}{d\varepsilon d\Omega}\right] \qquad (20)$$

where $f_s(\mathbf{p},\rho) = (1/2\pi m T_\perp(p,\rho))\exp(-\mathbf{p}_\perp^2/(2\pi m T_\perp(p,\rho)))F(p,\rho)$, $n_i(\rho)$ ion density, $\mathbf{v}_s$ supra thermal electron velocity, σ_{ei} is the electron-ion Bremsstrahlung cross-section, calculated according to the Bethe-Heitler-Elwert formula, and σ_{ee} is the electron-electron Bremsstrahlung cross-section, calculated with the Haug-Elwert formula (both are in the Born approximation).

The line averaged emissivity is calculated by integrating (20) along the line of sight taking into account the real geometry of the experiment (plasma configuration, position of lines of sight). The photon temperature is then deduced from the spectrum of the calculated emission for each line of sight.

6. CODE BENCHMARKING

The code has been benchmarked on a small number off well documented discharges from different operation regimes. All free parameters in the code are determined in these case studies and kept constant in subsequent modelling calculations.

I.Stochastic nature of ray trajectories.

In JET, typical ray trajectories extend over more than one pass before full absorption of the wave power is obtained even in a low density plasma ($n_{e0} \approx (1 \div 1.5) \times 10^{19} m^{-3}$) with a relatively high temperature. Trajectories corresponding to infinitesimally close initial conditions, diverge exponentially in phase space. This behaviour is called stochasticity. The stochasticity of ray trajectories and it's implication for the absorption of LH waves was investigated in [32-34]. Relatively low aspect ratio $R_0/a \cong 3$ and high ellipticity $1.15 < \kappa < 1.75$ result in poloidal asymmetry that is responsible for the ray stochastisity in JET. Another cause of the divergence of ray trajectories is the scattering of LH waves. Fig.2 shows the behaviour of ray trajectories and parallel refractive index in the case of propagation with and without scattering on density fluctuations in a high temperature plasma. The solid lines show the behaviour without scattering ($\Delta=0$, cf. Eq.(10)). The dashed lines are obtained with a scattering parameter $\Delta=0.25$.

II. Influence of diffusion and scattering on RF power deposition and driven current profile.

Modelling of LH current drive in a high temperature discharge was done for zero and non-zero electron diffusion and wave scattering (Fig.3). The best fit of the calculated to measured FEB signals was found for a diffusion coefficient $D_0 = 0.5 m^2/s$ and a parameter $\Delta \approx 0.25$, which were then used for all other calculations, unless indicated. The results of the calculations for the high temperature plasma for three different sets of diffusion coefficient and fluctuation amplitude are shown in Fig.4.

III. Influence of $T_\perp$ on RF power deposition, driven current and hard X-ray emission profiles.

The power deposition and current density profiles for distribution functions with different $T_\perp$ are shown in Fig.5. There is a moderate variation of the profiles for the wide range of $T_\perp$. The FEB brightness profile and X-ray photon temperature are shown in Fig.6 and Fig.7, for the same plasma parameters as in Fig.5. They are more sensitive to $T_\perp$ than P_{RF} and J_{RF}. Comparison of profiles in Fig.6 and Fig.7 shows, that calculated brightness and temperature are in a reasonable agreement with the experimental data under the assumption, that $T_\perp$ is

defined by equations (16-17) with $C_2 \cong 2$. This analysis shows that the information from FEB diagnostic is very valuable and essential for the validation of the model and the code.

7. ANALYSIS OF JET EXPERIMENTS

The parameters D_0, Δ, C_1, C_2 with the fixed values given in the previous section and equations (15-16) for the perpendicular tail temperature were used for the simulation of other discharges. These discharges cover a wide parameter range with densities $1.4*10^{19}\ m^{-3} \le n_{e0} \le 3.5*10^{19} m^{-3}$, temperatures $1.5keV \le T_{e0} \le 11keV$, magnetic fields $1.9T \le B_0 \le 3.1T$ and plasma currents $0.4MA \le I_p \le 3.1MA$.

The character of wave propagation varies significantly for the different shots. To illustrate this variation and its influence on the power deposition profile, shots with low temperature (multiple pass absorption) were chosen. The calculated driven current and power deposition profile for two different pulses (#24918: $T_{e0} = 1.5keV$, $n_{e0} = 1.7*10^{19} m^{-3}$, $B_0 = 3.35T$, $I_p = 0.37MA$, $\lambda(a) = 1.15$ and #24955: $T_{e0} = 2.3keV$, $n_{e0} = 2.8*10^{19} m^{-3}$, $B_0 = 3.2T$, $I_p = 1.5MA$ $\lambda(a) = 1.3$) are shown in Fig.8 and Fig.10, respectively. The calculated and experimental brightness and photon temperature profiles are shown in Fig.9 and Fig.11 for the same shots. The difference in the width of the power deposition, current and FEB profiles for the two discharges can be qualitatively explained by the difference in the propagation and absorption of the LH waves.

In the plasma with a small elongation and low temperature (shot #24918) rays experience many reflections. A typical ray trajectory and the behaviour of $n_{//}$ along this trajectory as a function of the radial coordinate ρ are shown in Fig.12a and Fig.12b, respectively (initial $n_{//}=1.85$ for this trajectory corresponds to the maximum in $P(n_{//})$). Some important feature of this behaviour can be deduced from a dispersion relation in the electrostatic approximation. It can be written in the following way:

$$n_r^2 = -\eta(B_{pol}n_{pol}/B + n_{tor})^2/\varepsilon - n_{pol}^2 \cong \omega_{pe}^3(B_{pol}n_{pol}/B + n_{tor})^2/\omega^2 - n_{pol}^2, \qquad (21)$$

where B_{pol} and B_{tor} are the poloidal and toroidal components of the magnetic field, n_{pol} and n_{tor} are the poloidal and toroidal components of the refractive index, respectively, and $n_r^2 = n_\perp^2 - n_{pol}^2$ (we assumed here that $B_{pol} / B_{tor} << 1$). The condition $\Phi \equiv (\omega_{pe}B_{pol}/(\omega B_{tor})) < 1$ is fulfilled in shot #24918. Dispersion relation (21) permits only a solution with the bounded $n_{//} \approx n_{pol}B_{pol}/B_{tor} + n_{tor}$ for LH waves with a given n_{tor} for such Φ [32,34,35]. Both mechanisms, toroidal upshift and wave scattering are complementary in the process of the spectral gap filling in this case. Due to low electron temperature and and a peaked radial profile absorption takes place close to the magnetic axis.

Shot #24955 is characterised by higher temperature and larger plasma elongation. The parameter Φ is greater than 1 in part of the plasma volume. Dispersion relation (21) permits a solution with unbounded $n_{//}$ for LH waves with a given n_{tor} in the region with $\Phi > 1$. The character of the wave propagation changes in this case, as illustrated in Fig.13a and Fig.13b, which show a typical ray trajectory and the evolution of $n_{//}$ along this trajectory as a function of the radial coordinate ρ (initial $n_{//}=1.85$). The ray trajectory rotates around the magnetic axis. Significant increase in $n_{//}$ occurs after the reflection of the wave from the boundary at the top of the plasma. Additional analysis shows that the bigger the elongation of the plasma the greater the increase in $n_{//}$ **[36]**. Absorption of the wave takes place at some distance from the centre. Consequently, the power deposition profile is hollow.

Table 1 shows a list of the major relevant parameters for the simulated shots. For a number of these shots the calculated FEB signals correspond to the experimental data (where available) for at least 6 central sight lines (from 10 available) with 30% accuracy. The qualitative similarity of the profiles is also observed. This is indicated by an 'A' sign. The sign 'N' is used for shots without experimental FEB data. For several shots with central density $n_{eo} \geq 2.10^{19}$ m^{-3} the calculated photon temperature and brightness profiles differ from the experimental data. Typically, they have a different shape and the calculated values are significantly higher than the experimental ones. These shots are indicated by a 'D'. The discrepancy in the calculated and experimentally observed FEB data in this case can be attributed to the intrinsic shortcoming of the model, based on the solution of the 1D Fokker-Planck equation. In the framework of this model, the perpendicular temperature is a prescribed parameter, calculated under the assumption, that the electron distribution function has a 'saturated plateau'. For a high density plasma and relatively low LH power this assumption breaks down. The calculated LH current (and efficiency) is higher in this case than what is observed experimentally.

On the other hand, for some cases where LHCD is combined with ICRH, the calculated photon temperature is significantly lower than the measured one. Fig.14 shows X-ray emission brightness and photon temperature profiles for such a discharge. The discrepancy in this case can be attributed to a synergistic effect between IC waves and the fast electron tail, produced by LH waves [35]. It can be explained in the following way. Single pass absorption of ICRF power in JET by electrons is negligible for IC waves with $n_{//} \leq 2$ in a Maxwellian plasma with temperature $T_{eo} \leq 10$keV. The number of fast electrons, which have the same parallel velocity as the parallel phase velocity of the IC wave, is very small. During LHCD a 'tail' on the distribution function is produced and the number of fast electrons, interacting with IC waves, can increase by many orders of magnitude. This tail should be extended in the presence of the ICRF power if the maximum parallel phase velocity of the IC waves is higher than the corresponding velocity of LH waves. The number of fast electrons and consequently

the current drive efficiency increase. This mechanism is not included into the model and it is not described by the code.

The current drive efficiency calculated by the code, $\eta = I_{LH}(MA)\langle n_e(10^{20}m^{-3})\rangle R_0(m)/P_{LH}(MW)$, as a function of the volume averaged temperature $\langle T_e(keV)\rangle$ is presented in Fig.15 (diamonds) for all shots listed in Table 1. The experimental LHCD efficiency η_{exp} deduced from the change in loop voltage is also shown in the same picture (squares), excluding shots where experimental data do not allow to infer η_{exp}. There is a large difference in the experimental and calculated values of the efficiency for temperature plasmas ($<T_e>\geq 2$keV). From the figure, it is evident, that there is a tendency of increasing efficiency with temperature for $<T_e>\leq 2.5$keV ($T_{e0}\leq 11$keV). The scatter of the points in the $<T_e>-\eta$ plane is partly connected with the difference in the shape of the T_e and n_e profiles.

Another reason for the large difference in efficiency in discharges with similar temperature is linked to the different level of the 'plateau saturation' produced by LH waves. Fig.16 and Fig.17 show the calculated electron distribution functions for shots #27745 and #24671 at t=54.5s, respectively. Each curve corresponds to a different radial position. Condition $D_{ql}(p_{\parallel},\rho)p_{\parallel}^3 \gg \nu_{ei} p_e^5$ is fulfilled for most of the region $v_1(\rho) < p_{\parallel}/\gamma < v_2(\rho)$ in shot #27745. The 'saturated plateau' is well pronounced in Fig.16. The calculated LHCD efficiency for this case is depicted by a cross in Fig.15. It is one of the highest efficiencies in Table 1. In contrast to a previous case, condition $D_{ql}(p_{\parallel},\rho)p_{\parallel}^3 \geq \nu_{ei} p_e^5$ is satisfied in a significant part of the velocity range $v_1(\rho) < p_{\parallel}/\gamma < v_2(\rho)$ for shot #24671. From Fig.17 it is seen, that the plateau is not well developed in shot #24671. In this case large part of the power is absorbed by relatively slow electrons ($v \geq v_1$), which have much larger collisionality than electrons with higher velocities ($v \leq v_2$). As a consequence, the calculated efficiency is relatively low. It is indicated in Fig.15 by a circle. Comparison of the parameters of the shots #27745 and #24671 (t=54.5s) reveals, that the major difference between them is the plasma density. For the higher density (#24671, t=54.5s) the LH power is insufficient to produce a 'saturated plateau'.

Taking into account the empirical dependence of η on $\langle T_e(keV)\rangle$, it is instructive to calculate the magnitude of $\xi = I_{LH}(MA)/(P_{LH}(MW)\langle T_e(keV)\rangle)$ as a function of the volume averaged density $< n_e >$. The corresponding points are shown in Fig.18 for all shots from Table 1. From the definition we can expect a density dependence $\xi \propto < n_e >^{-1}$ .The best fit of this function by the power approximation gives $\xi = 0.29 < n_e >^{-1.34}$, which is also shown in Fig.18. A faster decrease in ξ with density than $< n_e >^{-1}$ is qualitatively in agreement with the change in η (and consequently ξ) with LH power. The power level was limited to 2.35MW for all shots listed in Table 1. For shots with higher density the launched LH power was insufficient for the production of a 'saturated plateau'. The points corresponding to shots #27745 and #24671 (t=54.5s) are marked by cross and open circle, respectively.

VIII. PREDICTION OF LH CURRENT DRIVE IN ITER

A prediction of the capability of LHCD in ITER is made by means of the LHCD code described here. Our particular interest aims at investigating the so called 'advanced scenario'. Its main features are steady state operation with relatively low plasma current (I_p=13.5 MA) and large portion of bootstrap current ($I_b/I_p \approx 0.7$), high poloidal beta ($\beta_p \approx 3$) and high normalised beta ($\beta_N \approx 3-4$). A temperature profile of the triangular type with T_{e0} = 15keV and a rather broad density profile, close to $n_e(\rho) = n_{e0}(1-(\rho/a)^2)^{0.25\div0.3}$ with n_{e0} =1.24 $10^{20}m^{-3}$ were chosen for the simulations. Fig.19 shows the LH current and power deposition profile for the case, when 50 MW of LH power at a frequency of 8GHz is injected with a top launcher with maximum $P(n_{//})$ peaked at $n_{//}$=2 and with half width of 0.1. The total driven current is 2.08MA and the current drive efficiency $\eta = I_{LH}(MA)\langle n_e(10^{20}m^{-3})\rangle R_0(m)/P_{LH}(MW)$=0.31. The maximum of the current is driven near ρ = .56a and it drops to zero at ρ = 0.32a. This location is favourable for the 'advanced scenario' [38]. For a lower frequency (f=5.5GHz) the LH driven current decreases slightly to 1.92MA and the maximum of $J_{RF}(\rho)$ shifts to ρ = 0.6a.

CONCLUSIONS

A code for the simulation of LHCD in tokamaks has been developed. The code is based on a model, which incorporates the stochastic diffusion of fast electrons with $D_{\rho\rho} = D_m v_{//}/v_e$, the scattering of LH waves by low frequency fluctuations and an analytical approximation for $T_\perp$. It was benchmarked by comparing the numerical simulations with the experimental data obtained on JET. The comparison shows that the LHCD code with the fixed coefficients describes a number of JET discharges reasonably well. The discharges cover a large range in electron temperature: 1.4-9keV and in electron density: 1.4 to 3. $10^{19}m^{-3}$. The validation of the code gives confidence for its application to predictive modelling of LH experiments, both for JET and ITER. A simulation of LHCD in ITER shows that LH current can be driven in the mid radius area with an efficiency of about 0.31. Steady state operation in a scheme of LHCD combined with high bootstrap current is possible.

ACKNOWLEDGEMENT

Authors are grateful to Dr.V.Parail for very fruitful discussions and suggestions.

REFERENCES

[1] Bonoli, P.T., Ott, E., Phys. Fluids 25 (1982) 359

[2] Baranov, Y.F., Fedorov, V.I., Pis'ma Zh. Tekh. Fiz. 4 (1978) 800 [Soviet Phys.Tech.Phys.Lett. 4(1978) 322], Nucl. Fusion 20 (1980) 1111

[3] Ignat, D.W., Phys. Fluids 24 (1981) 1110

[4] Bonoli, P.T., Englade, R.C., Phys.Fluids 29 (1986) 2937

[5] Brambilla, M., Comput.Phys.Rep. 4 (1986) 71

[6] Baranov, Y.F., Esterkin, A.R., Sov.J.Plasma Phys. 16 (1990) 665

[7] Bonoli, P.T., Porkolab, M., Takase, Y., Knowlton. S.F., Nucl.Fusion 28 (1988) 991

[8] Devoto, R.S., Blackfield, D.T., Fenstermacher, M.E., et al., Nucl.Fusion 32 (1992) 773

[9] Kesner, J., Paoletti, F., Bernabei, S., et al., Nucl.Fusion 34 (1994) 619

[10] Ignat, D.W., Valeo, E.J., Jardin, S.C., Nucl.Fusion 34 (1994) 837

[11] Fuchs, V., Bonoli, P.T., Shkarofsky, I.P., et al., Nucl.Fusion 35 (1995) 1

[12] Pereversev, G.V., Nucl.Fusion,32 (1992) 1091

[13] Vahala, L., Vahala, G., Bonoli, P.T., Phys.Fluids 4 (1992) 4033

[14] Karney,C.F.F., Fisch, N.J., Phys. Fluids 22, 1817 (1979).

[15] Fuchs, V., Cairns, R.A., Shoucri, M.M., Hizanidis, K., Bers, A., Phys.Fluids 28 (1985) 3619

[16] Baranov Y.F., Brusati, M., Ekedal, A., Froissard, P., Gormezano, C., Lennholm, M., Rimini, F., 20th EPS Conf. on Controlled Fus. and Plasma Phys. Lisbon, (1993) 881.

[17] Girussi, G., Plasma Phys. Controlled Fusion 35 (1993)A123

[18] McKenzie, J.S., O'Brien, M.R., Cox, M., Comp.Phys.Communications 66 (1991) 194

[19] McCormick, K., Soldner, F.X., Eckhart, D., et al., Phys.Rev.Lett. 58 (1987) 491

[20] Soltwisch, H., Rev. Sci. Instrum. 57 (1986) 1939

[21] Kararian-Vibert, F., Litaudon, X., Arslanbekov, R., et al., Proc. 22nd EPS Conf. on Controlled Fusion and Plasma Phys, Bournemouth, England, IV (1995) 373

[22] Froissard, P., et al., Proc. 18th EPS Conf. on Controlled Fusion and Plasma Phys, Berlin, III (1991) 389.

[23] Brusati, M., Bartlett, D.V., Ekedal, A., et al., Nucl.Fusion 34 (1994) 23

[24] Ott, E., Phys. Fluids 22 (1979) 1732

[25] Slusher R.E., Surko C.M., Phys. Rev. Lett.40 (1978) 400 Surko C.M., Slusher R.E., Phys.Fluids 23 (1980) 2425

[26] Liewer P.C. Nucl.Fusion 25 (1985) 543

[27] Fisch, N.J., Rev of Modern Phys. 59 (1987) 175

[28] Shoucri, M., Shkarofsky I., CCFM RI , 401e (1993)

[29] Zakharov, L.E., Method of electrodynamic moments for calculation of equilibrium of the toroidal plasma. Preprint of Atomic Energy Institute, Moscow, 4114/6, 1985

[30] Lao, L.L., Ferron, J.R., Groebner, R.J., et al., Nucl. Fusion 30 (1990) 1035
[31] Litaudon, X., Moreau, D., Nucl.Fusion 30 (1990) 471
[32] Esterkin, A.R., Piliya, A.D., Plasma Phys. Controlled Fusion 34 (1992) 1957
[33] Kupfer, K., Moreau, D., Nucl.Fusion 32 (1992) 1845
[34] Kupfer, K., Moreau, D., Litaudon, X., Phys.Fluids B, 5 (1993) 4391
[35] Baranov, Y.F., Piliya, A.D., Esterkin, A.R., JETP Lett. 51 (1990) 701
[36] Esterkin, A.R., Piliya A.D., Nucl.Fusion 32 (1992) 927
[37] Gormezano, C., 10th Topical Conf. on RF Power in Plasmas. Boston 1993
[38] Soldner, F.X., Baranov, Y.F., Bhatnagar, V.P., et al., Proc. 21th EPS Conf. on Controlled Fus. and Plasma Phys. Montpellier, (1994) 1126
[39] Pasini, D., Gill, R.D., Holm, J., et al., Rev. Sci. Instrum. 59 (1988) 693

TABLE 1

Shot No.	Time Slice	n_{e0} ($10^{19}m^{-3}$)	T_{e0} (keV)	B_0 (T)	Ip (MA)	P_{LH} (MW)	P_{ICRH} (MW)	I_{LH} (MA)	Comp. of FEB data	$<n_e>$ ($10^{19}m^{-3}$	$<T_e>$ (keV)	Z_{ef}	η
24200	58.5	1.6	3.7	3	1.5	0.87	0	0.47	A	0.9	1.4	1.63	0.15
24659	53	2.4	4.5	2.9	2	1.6	2.19	0.42	A	1.6	1.5	2.6	0.13
24671	47	1.5	7	2.9	2	1.42	5	0.71	A	1.1	1.8	3.2	0.17
24671	54	3.5	7	2.9	2.1	1.43	5.1	0.23	D	1.7	2.1	3.5	0.08
24875	77	1.9	4.8	2	2	0.97	2.63	0.35	D	1.5	1.7	1.5	0.16
24887	76	2.5	1.7	1.9	2	0.86	0	0.054	A	1.75	0.6	1.5	0.03
24896	50.5	2.6	5	2.6	2.1	1.37	4.15	0.48	D	1.9	1.7	1.8	0.20
24898	53	2.8	5.3	2.6	2.1	1.69	3.77	0.44	A	1.8	2	2.2	0.14
24918	50	1.7	1.5	3.4	0.4	1.8	0	0.2	A	1.03	0.3	1.6	0.03
24951	52	3	3	2.1	2.7	2.04	0	0.45	A	1.8	1.4	2	0.12
24955	51.4	2.8	2.3	3.2	1.5	2.36	0	0.37	A	1.7	1.1	1.7	0.08
24966	51.5	2.2	9	3.1	1.6	2.4	3.35	1.02	D	1.8	2	3	0.23
25350	58	2.2	3	2.9	1.5	1.7	0	0.42	N	1.4	1.6	2	0.10
25376	51	2.2	8.9	3.2	1.5	2.2	4.1	0.75	N	1.2	2	3.5	0.12
25380	49.5	2.8	11.1	3.2	2	2.24	4.1	0.56	N	1.7	2	4.2	0.13
26564	54	2.6	5.2	2.6	1	1.61	3.5	0.21	N	1.8	1.2	2	0.07
27684	60	2.6	4.8	2.6	1.5	1.65	3.83	0.33	D	1.7	1.5	2.5	0.10
27718	53.5	2.5	4.2	3.3	1.6	1.64	0	0.33	A	1.1	1	3.7	0.07
27745	52	1.4	8	3.3	3.1	1.36	0.05	1.2	A	0.9	2.5	3.8	0.24

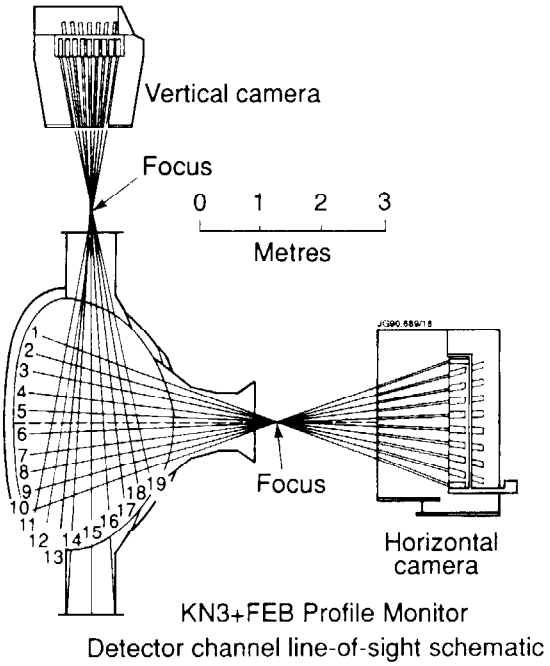

Fig. 1. Layout of the Fast Electron Bremsstrahlung diagnostic.

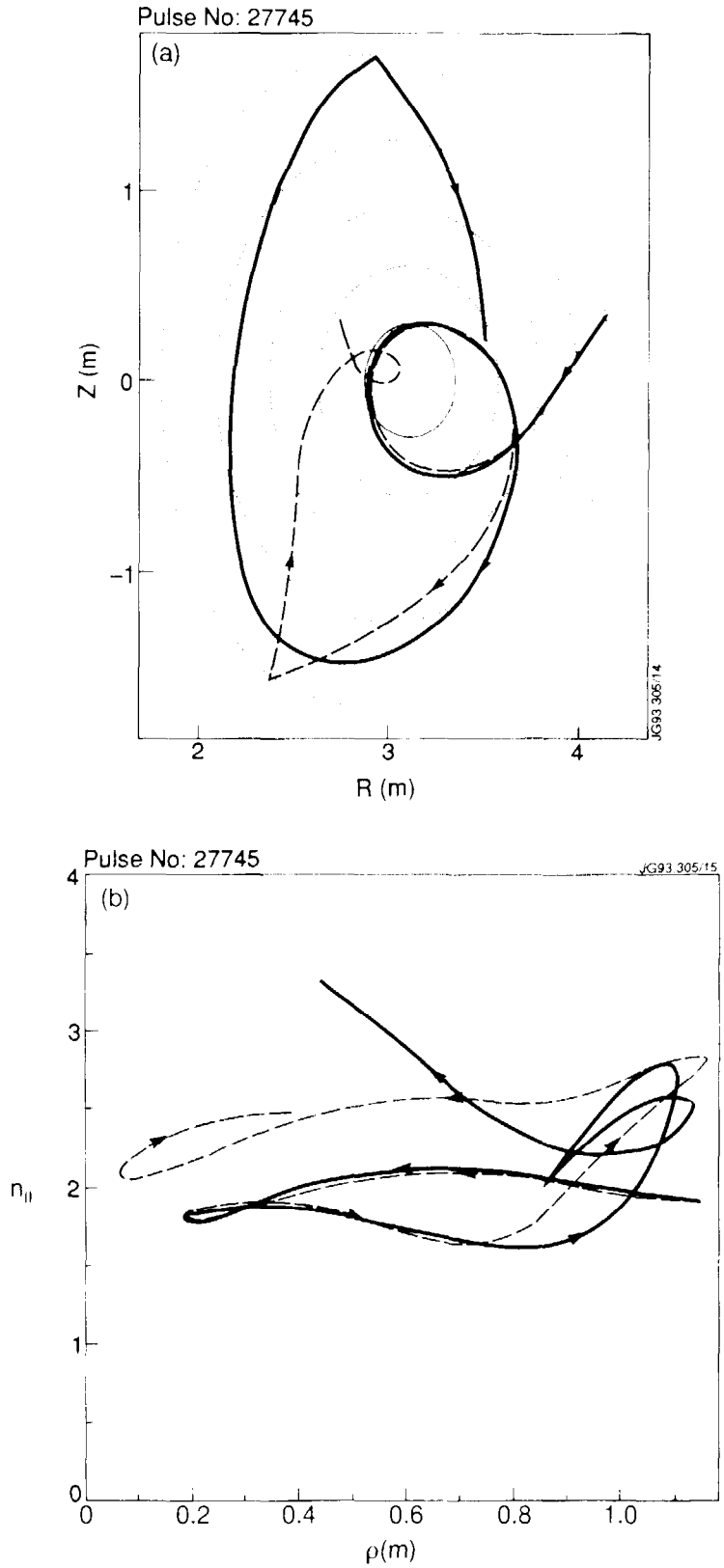

Fig. 2. a: Projection of the ray-trajectories on the poloidal cross-section. b: Behaviour of $n_{//}$ along trajectories as a function of radial position ρ . Solid line: without scattering, dashed line: with scattering, Δ =0.25. Pulse #27745.

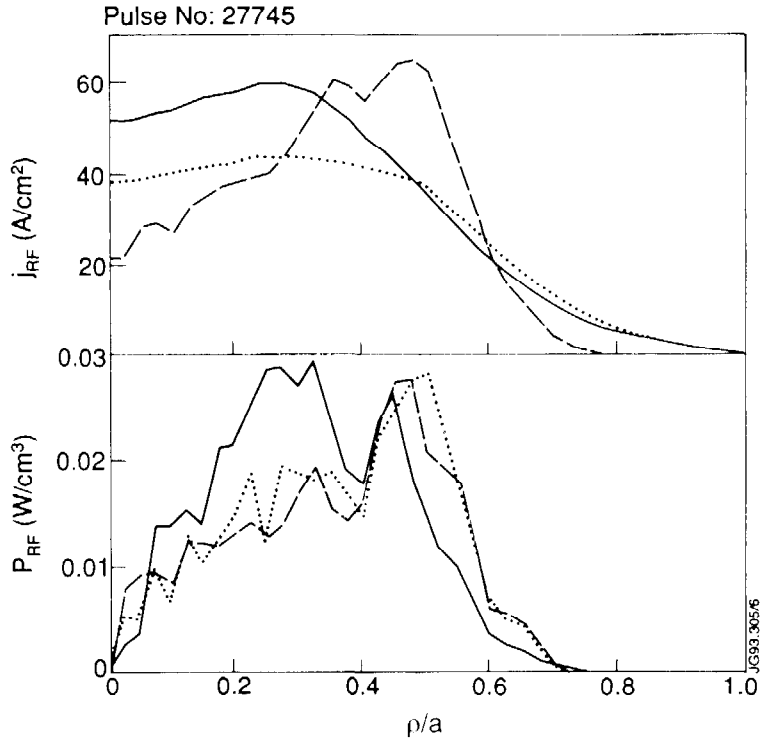

Fig. 3. The calculated LH driven current density $j_{RF}(\rho/a)$ and dissipated RF power density $P_{RF}(\rho/a)$ for zero and non-zero diffusion and scattering. Pulse #27745. Solid lines: Δ = 0.25, D_o=0.5m^2/s, dashed line: Δ =0, D_o= 0, dotted line: Δ =0, D_o= 0.5m^2/s, C_2=2.

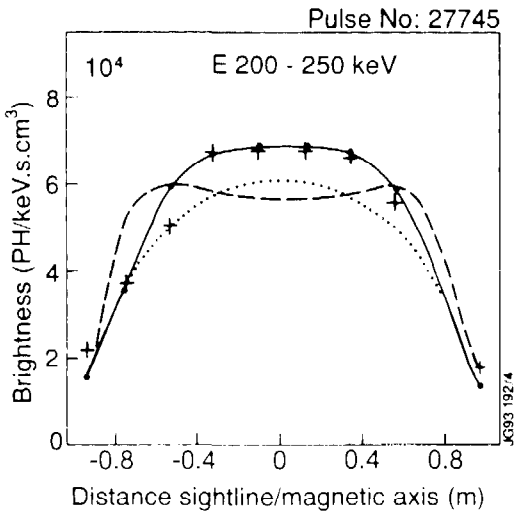

Fig. 4. Profiles of the calculated and experimentally observed brightness. Pulse #27745. Solid lines: Δ =0.25, D_O= 0.5m^2/s, dashed line: Δ =0, D_O=0, dotted line: Δ =0, D_O=0.5m^2/s, C_2=2, crosses: experimental data.

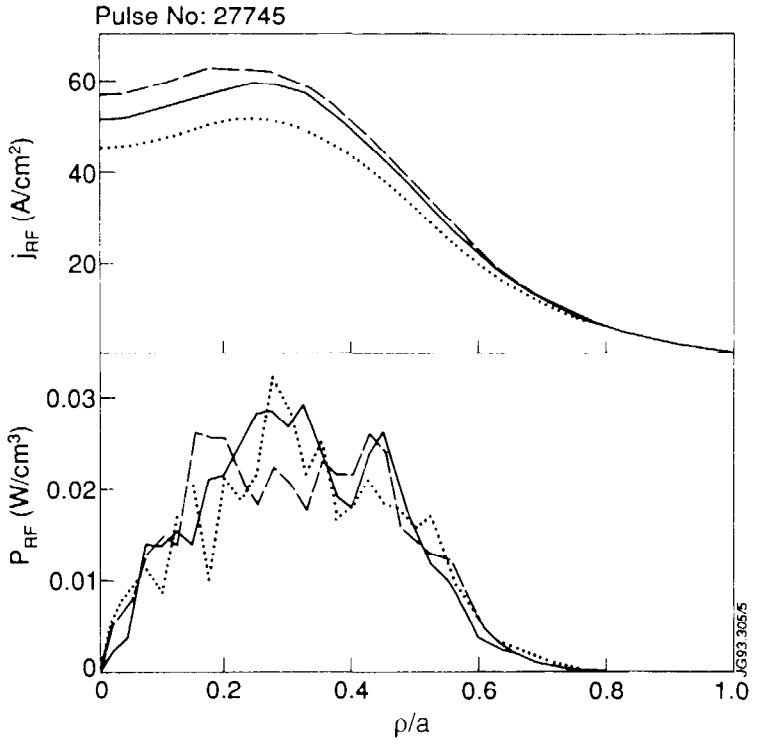

Fig. 5. The calculated LH driven current density $j_{RF}(\rho)$ and dissipated RF power density $p_{RF}(\rho)$ for different values $T_{\perp}$. Pulse #27745. Solid lines: C_2=2, dashed line: C_2=4, dotted line: C_2=1.

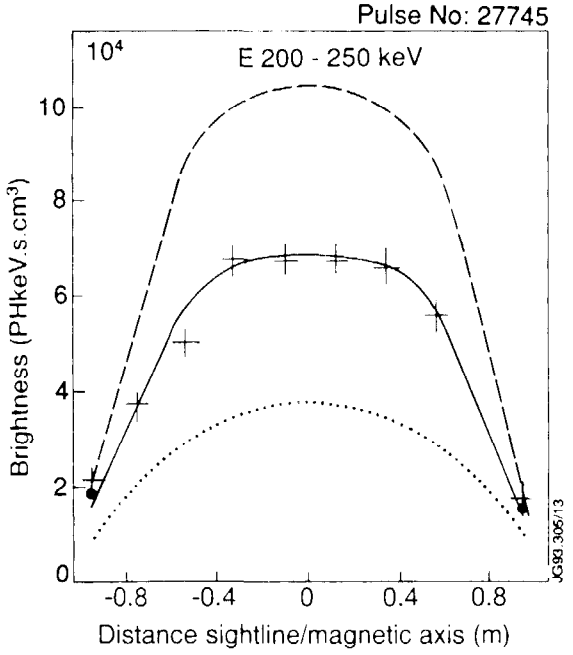

Fig. 6 Profiles of the calculated and experimentally observed brightness. Pulse #27745. Solid line: C_2=2, dashed line: C_2=4, dotted line: C_2=1, crosses: experimental data.

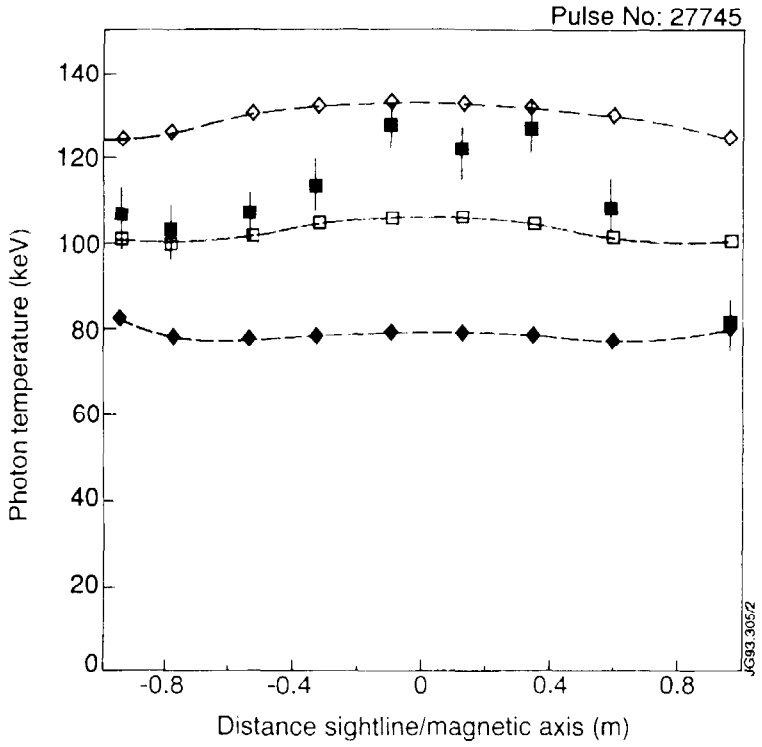

Fig. 7. Profiles of the calculated and experimentally observed photon temperature. Pulse #27745. Open square: C_2=2, open diamond: C_2=4 , solid diamond: C_2=1, solid square: experimental data.

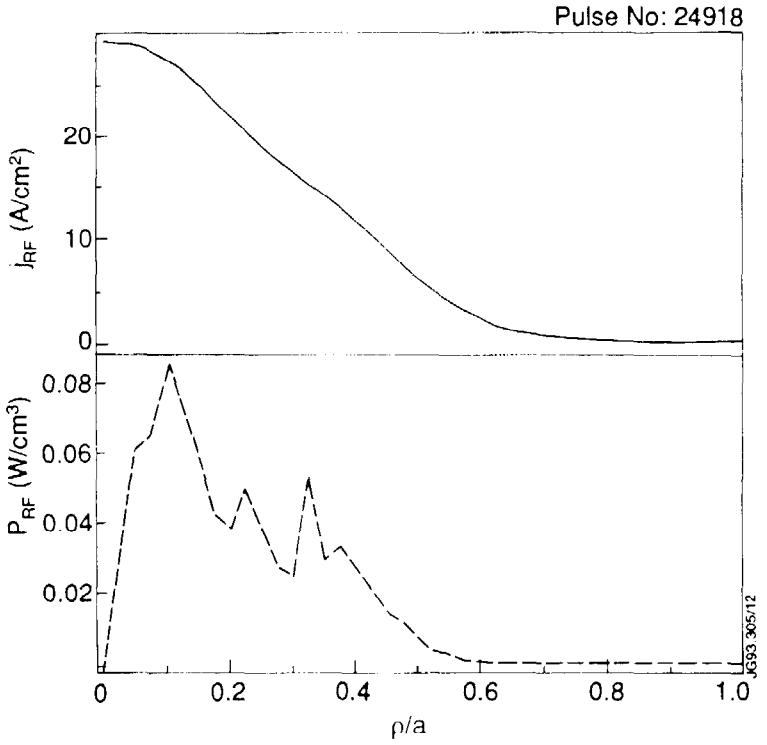

Fig. 8 The calculated LH driven current density j_{RF} (ρ) and dissipated RF power density p_{RF}(ρ). Pulse #24918.

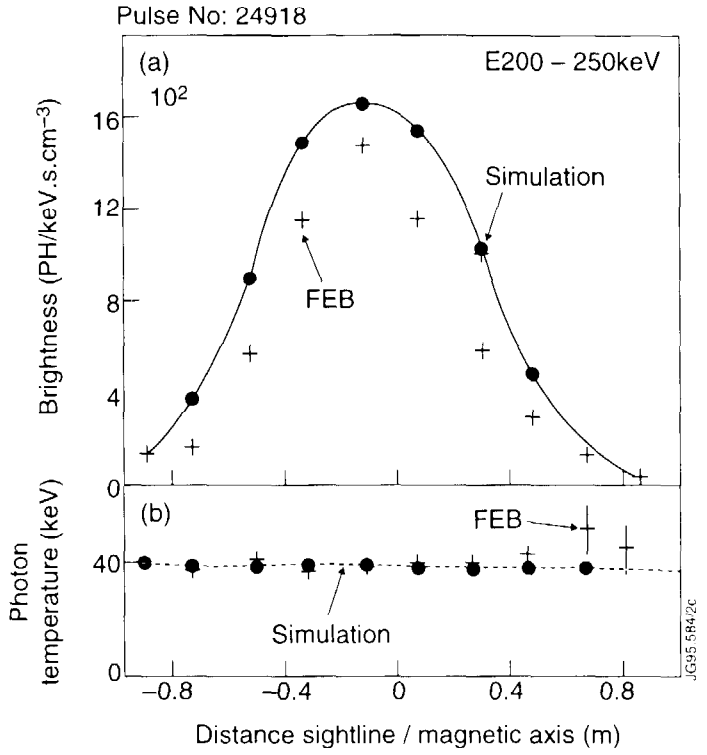

Fig. 9. Profiles of the calculated and experimentally observed X-ray emission. a: brightness, b: photon temperature. Pulse #24918.

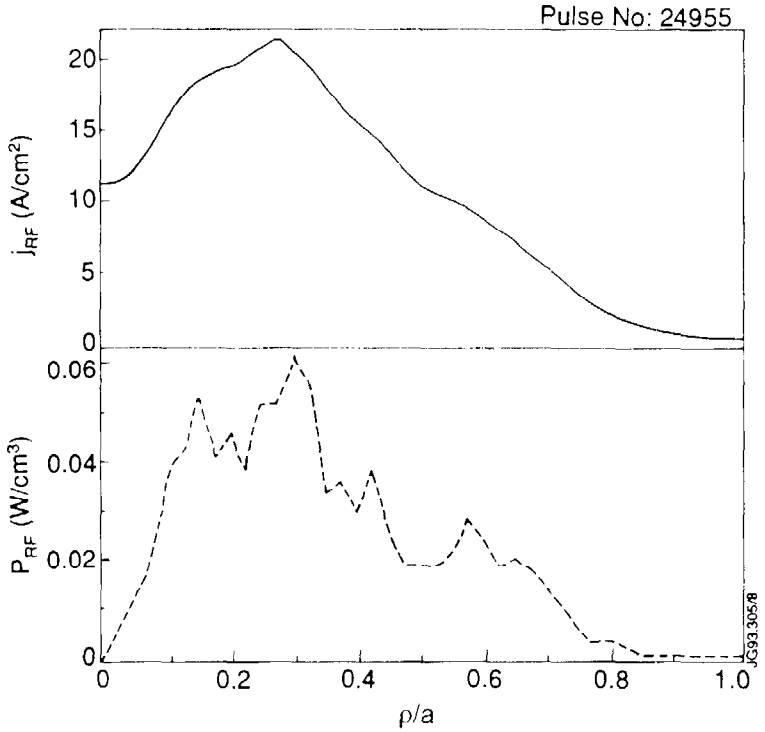

Fig. 10. The calculated LH driven current density $j_{RF}(\rho)$ and dissipated RF power density $p_{RF}(\rho)$. Pulse #24955.

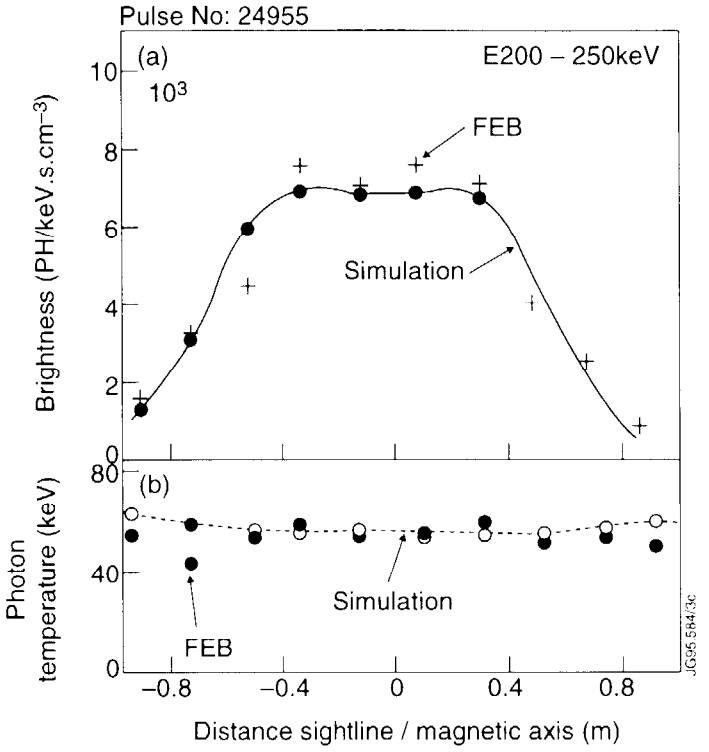

Fig. 11. Profiles of the calculated and experimentally observed X-ray emission. a: brightness, b: photon temperature. Pulse #24955.

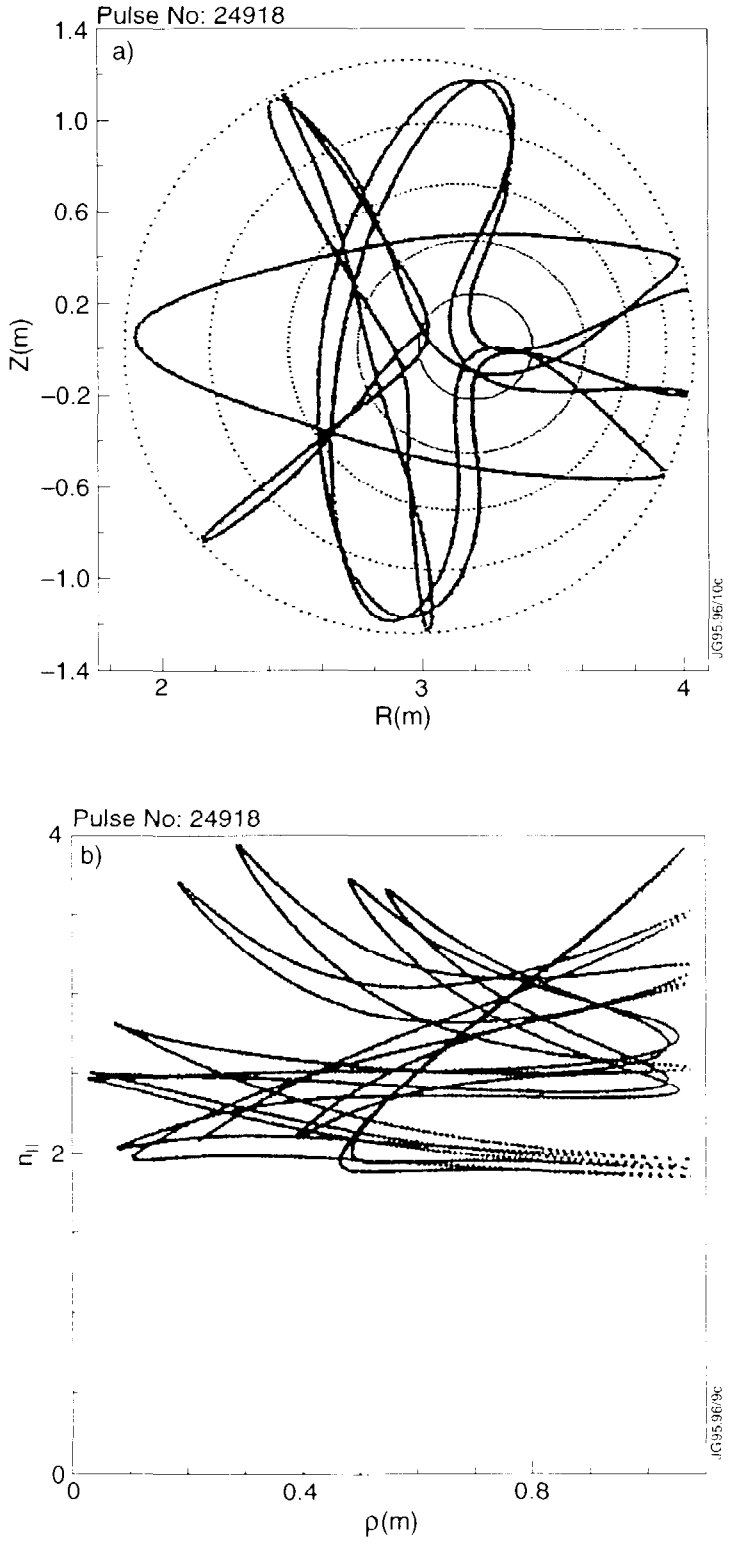

Fig. 12. a: Projection of the ray-trajectories on the poloidal cross-section. b: Behaviour of $n_{//}$ along the trajectories as a function of radial position ρ . Pulse #24918.

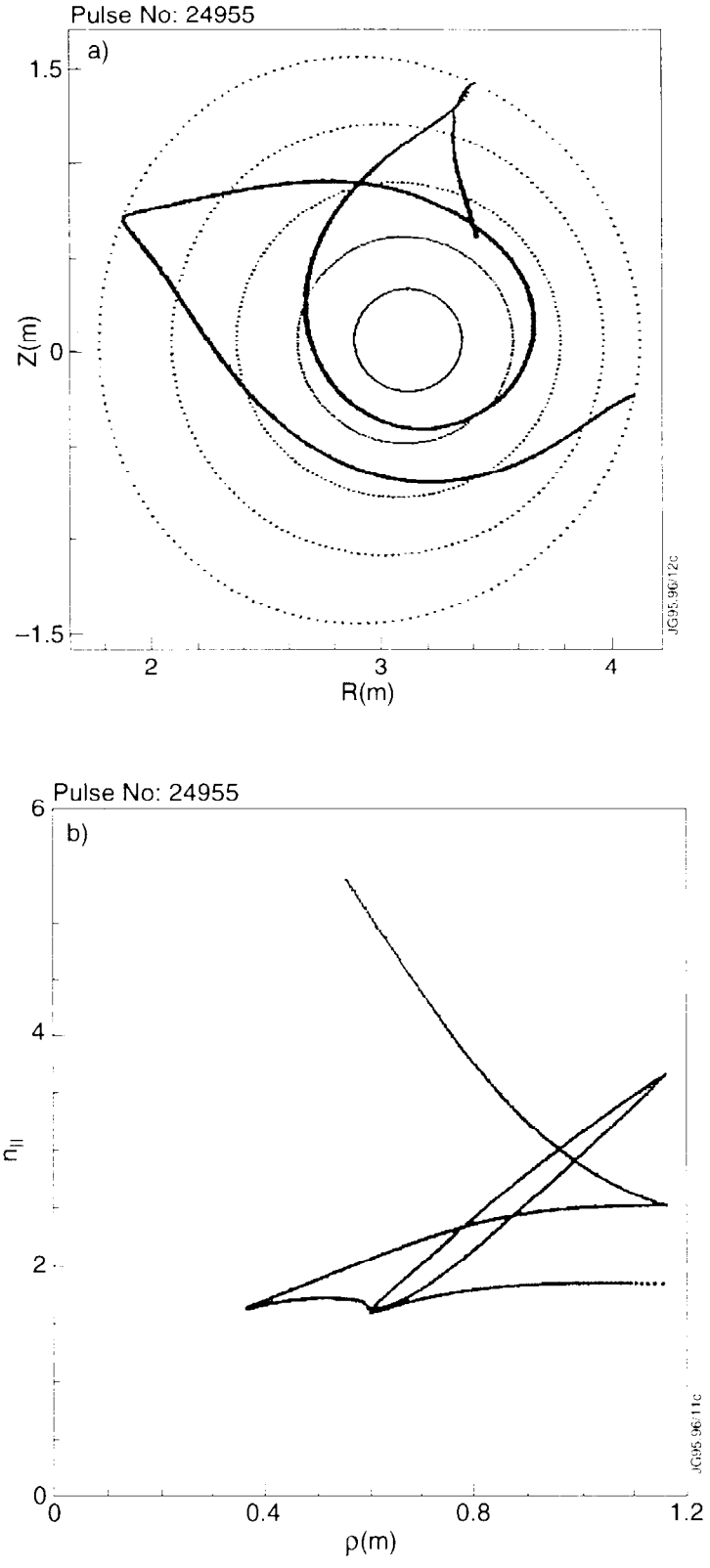

Fig. 13. a: Projection of the ray-trajectories on the poloidal cross-section. b: Behaviour of $n_{//}$ along the trajectories as a function of radial position ρ . Pulse #24955.

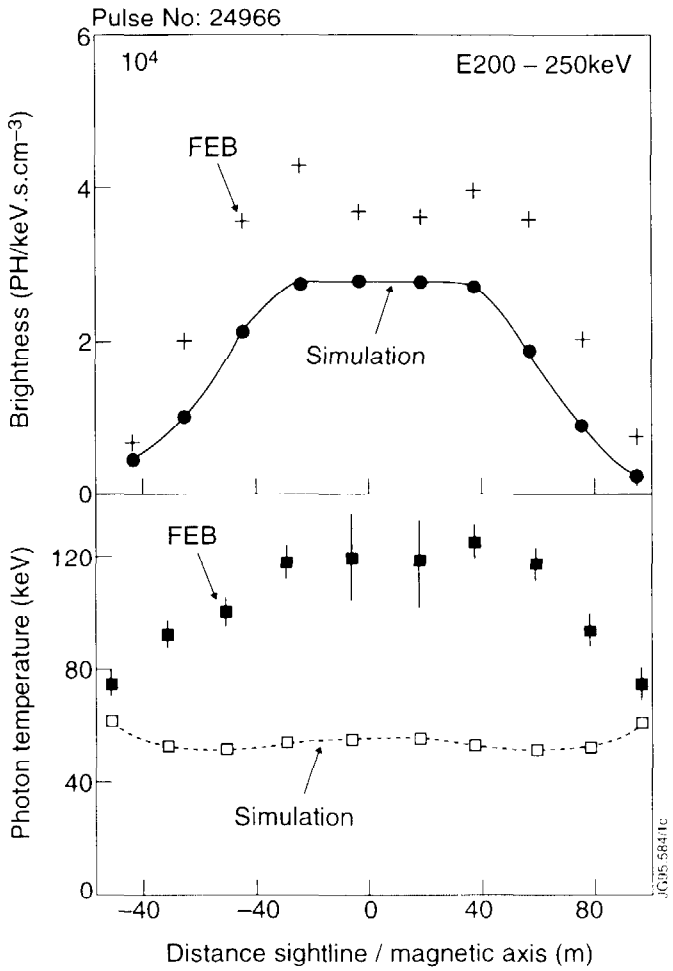

Fig. 14. Profiles of the calculated and experimentally observed X-ray emission. a: brightness, b: photon temperature. Pulse #24966.

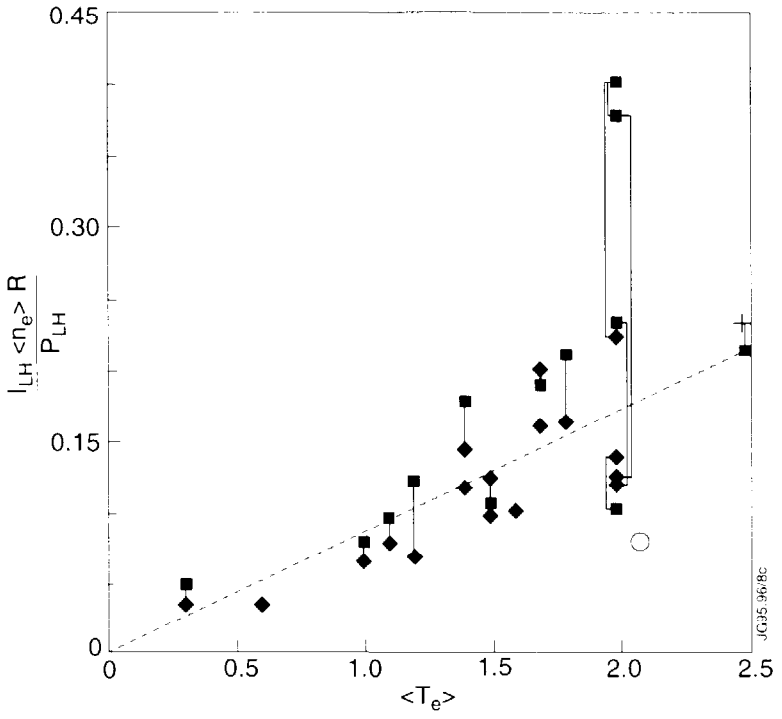

Fig. 15. Dependence of the calculated (diamonds) and experimental (squares) efficiency on volume averaged electron temperature for different pulses. Points for the calculated and experimental efficiencies are connected for corresponding pulses. Dashed line is the best fit for the calculated efficiency by the power approximation. Calculated efficiency for pulse #27745 (cross), pulse #24671(circle).

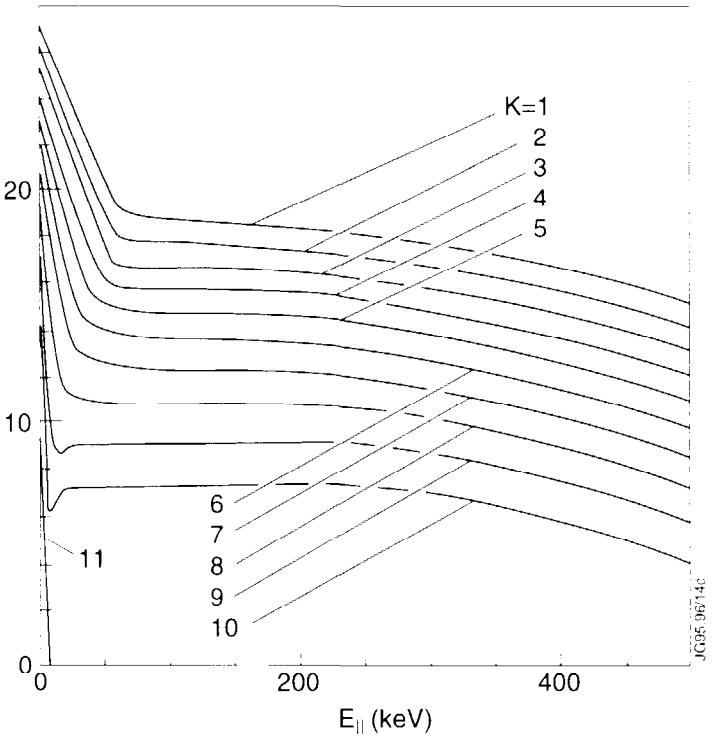

Fig. 16. Dependence of $ln[F(E_{//}, \rho_k)*exp(-k-1)]$ on kinetic energy $E_{//} = mc^2(\gamma(p_{//}) - 1)$, where $F(E_{//}, \rho_k)$ -the electron distribution function $\gamma^2(p_{//}) = 1 + (p_{//}/mc)^2$, $\rho_k = a(k-1)/10$. Pulse #27745.

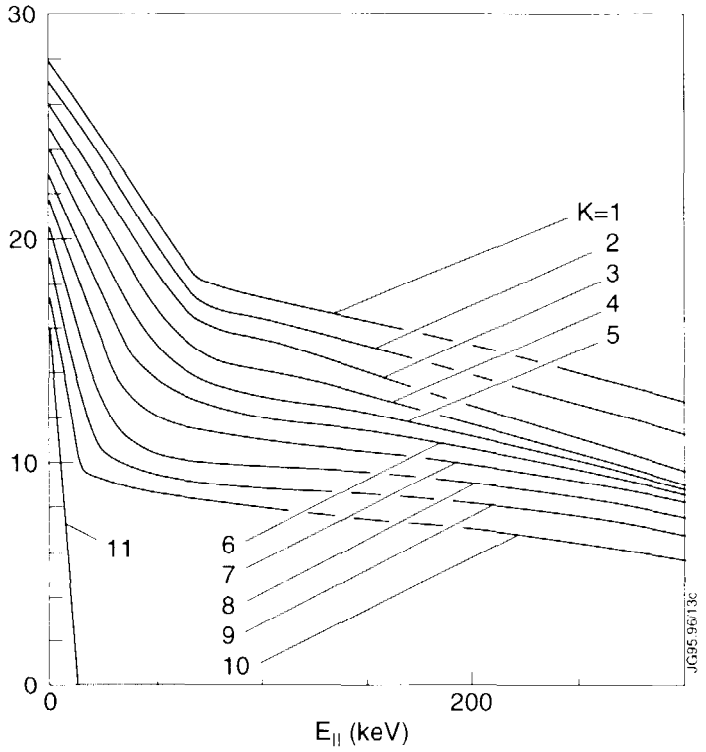

*Fig. 17. Dependence of ln[$F(E_{//}, \rho_k$)*exp(-k-1)] on kinetic energy $E_{//} = mc^2(\gamma(p_{//})-1)$, where $F(E_{//}, \rho_k)$ is the electron distribution function, ρ_k=a(k-1)/10. Pulse #24671, t=54.5.*

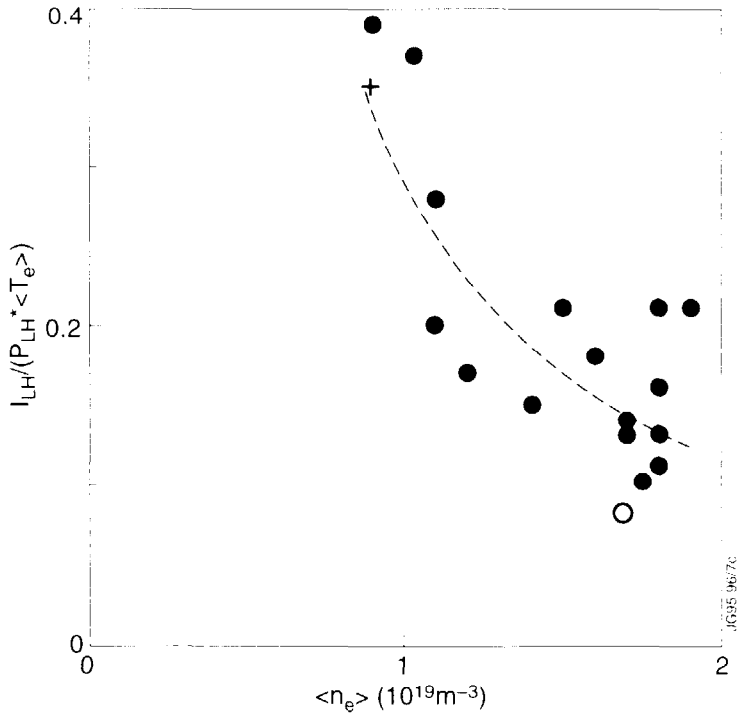

Fig. 18. Dependence of $\xi = I_{LH}(MA)/(P_{LH}(MW)\langle T_e(keV)\rangle)$ on volume averaged temperature for different pulses . Dashed line is the best fit by the power approximation. Cross: pulse #27745, diamond: pulse #24671.

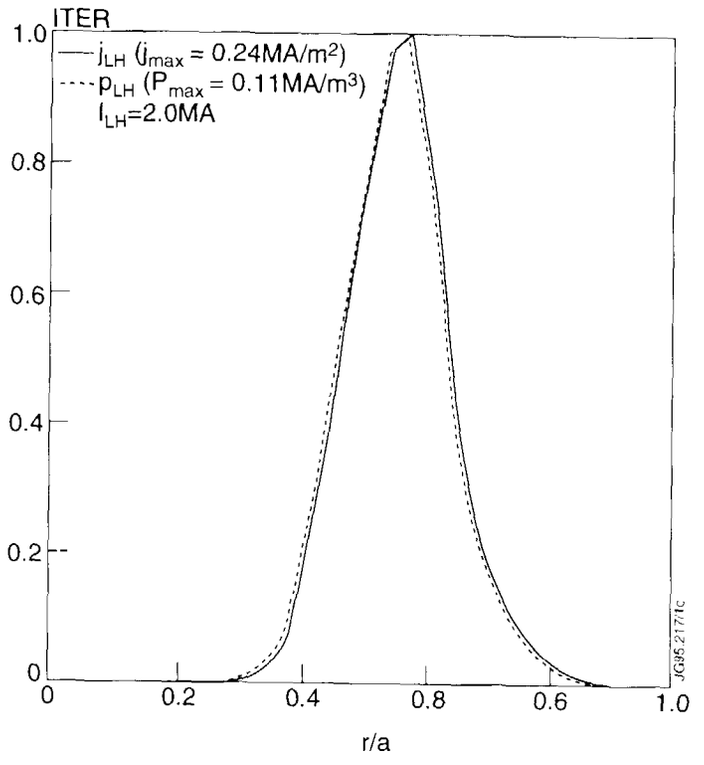

*Fig. 19. The calculated LH driven current density $j_{RF}(\rho)$ and dissipated RF power density $p_{RF}(\rho)$ in an ITER like discharge. R_o=7.75m, a = 2.77m, k=1.66, B_T=6.2T, I_p=13.5MA, T_{eo}=15keV, n_{eo}=1.24*10^{19}m^{-3}, $N_{//Pmax}$=2., $N_{//FWHM}$=0.1, P_{LH}=50MW, f=8.GHz. Total LH driven current 2.08MA.*